

An error estimate on the direct inversion model in shear stiffness imaging

This article has been downloaded from IOPscience. Please scroll down to see the full text article.

2009 Inverse Problems 25 075003

(<http://iopscience.iop.org/0266-5611/25/7/075003>)

[The Table of Contents](#) and [more related content](#) is available

Download details:

IP Address: 128.113.82.223

The article was downloaded on 16/09/2009 at 14:47

Please note that [terms and conditions apply](#).

An error estimate on the direct inversion model in shear stiffness imaging

Kui Lin and Joyce McLaughlin

Mathematics Department, Rensselaer Polytechnic Institute, 110 8th Street, Troy, NY 12180, USA

E-mail: link@rpi.edu and mclauj@rpi.edu

Received 6 September 2008, in final form 17 March 2009

Published 26 May 2009

Online at stacks.iop.org/IP/25/075003

Abstract

This paper considers an inverse problem of shear stiffness imaging in a linear isotropic two-dimensional acoustic media, where the targeted parameter is the shear modulus μ . For given single component displacement data, the mathematical model to recover the shear modulus appears to be a first-order partial differential equation while a much simpler algebraic model, called the direct inversion, can be derived by eliminating the first derivative terms of the shear modulus from the partial differential equation model. The objective of this paper is to establish a theoretical bound on the relative difference between the true value of the modulus and the approximated value reconstructed from the direct inversion. We exhibit a quantitative estimate of the relative error and present reconstruction examples by the direct inversion from simulated data. We demonstrate that the relative error of the numerical solution is well bounded by the theoretical error estimate.

(Some figures in this article are in colour only in the electronic version)

1. Introduction

Shear stiffness imaging is targeted here because shear wave speed is 2–4 times larger in abnormal tissue than normal tissue. We expect that shear stiffness imaging in combination with ultrasound imaging can provide more accurate diagnosis of cancerous tumors. There have been four experiments proposed to detect shear stiffness variations:

- *Static experiment*: the tissue is compressed;
- *Acoustic radiation force imaging (ARFI)*: focused acoustic pulses are used to generate interior sources of displacement; from each pulse a radial wave propagates;
- *Dynamic excitation*: a time harmonic excitation made on the boundary or in the interior creates a time harmonic wave in the tissue;

- *Transient experiments:* (1) a time-dependent pulse on the boundary, or along a line in the interior, creates a propagating wave in the interior; (2) two harmonic excitations at two different points, each excited at two nearby but different frequencies, generates a traveling wave.

For most of these experiments, ultrasound [1–9, 12, 14, 16–19, 26, 27, 29, 30, 35–37] or magnetic resonance imaging [13, 21, 23–25, 28, 31–34] is used to measure the interior displacement on a fine grid of points. The aim is to create images of shear wave speed from displacement data.

For a detailed review of the experiments, see [22]. In this paper, our focus is on the dynamic excitation experiments and the transient experiments where single frequency elastography data can be measured. External or internal mechanical stimulation of the target media is applied in both experiments. A time harmonic excitation is used in the dynamic experiments while the setup for the transient experiments is that the tissue is initially at rest and then excited by a broadband pulse with central frequency 50–200 Hz. There are two types of waves propagating away from the excitation: a compression wave, which displaces tissue parallel to the direction of wave propagation, and is comparatively fast with speed approximately 1500 m s^{-1} and a shear wave, which displaces tissue orthogonally to the direction of wave propagation, and is comparatively slow with speed approximately 3 m s^{-1} .

We use several features of these two types of experiments to facilitate the mathematical modeling. First, the amplitude of the shear wave is on the order of microns and the stress–strain curve has been shown to be approximately linear in [26]. This enables us to use the linear equations of elasticity. Second, the compression wave has long wavelength, is slowly varying and has low amplitude relative to the shear wave. So we treat the compression wave as noise in the data and assume that one measured component of the elastic wave satisfies a wave equation, see [22] for more discussion about this approximation.

Thus in this paper, we consider the following inverse problem: under the assumption that the acoustic wave equation $\nabla \cdot (\mu \nabla u) = \rho_0 u_{tt}$ is a good model for our dynamic experiments, then determine the shear modulus from the Fourier transform $\hat{u}(x, \omega)$ of the interior displacement data $u(x, t)$. Here we use the commonly accepted hypothesis that the density ρ_0 is a known constant.

The mathematical model for the inverse problem appears to be a first-order partial differential equation for the modulus, μ . A widely accepted and considerably simpler model to recover μ is called the direct inversion model and is obtained by making the locally constant assumption on the targeted value and removing the terms in the inverse problem containing the first derivatives of μ . Some remarkable reconstruction results have been obtained using a number of different implementations of the direct inversion model [1, 2, 8, 10, 12, 21, 23–26, 28], with also application to a variety of different experiments. Motivated by these successful applications of the direct inversion model, we investigate the locally constant assumption for μ and establish theoretically a bound on the relative difference between the true modulus μ and the direct inversion approximation, $\hat{\mu}$. In this paper, we present the quantitative error bound and demonstrate: (1) the key elements that determine the relative error between the true value and the approximated value; (2) the appropriate scenarios where the direct inversion model can be applied; and (3) the normal circumstances when the simple algebraic equation of the direct inversion model will fail.

The remainder of this paper is organized as follows. In section 2, we discuss the mathematical models for forward and inverse problems in detail. Section 3 is devoted to the derivation of the bound for the relative difference between the true modulus μ and the direct inversion approximation, $\hat{\mu}$. In section 4, we (1) discuss the numerical simulation setup and the implementation of the absorbing boundary condition for the forward problem and

(2) present theoretical results of the numerical error control for the inverse problem. Then in section 5 we present shear modulus reconstructions by the direct inversion from the simulated data. We conclude this document in section 6 with remarks on future work.

2. Mathematical models for the forward and the inverse problem

2.1. Forward problem model

Assume that the density $\rho \in C^1(\bar{\Omega})$ and the shear modulus $\mu \in C^2(\bar{\Omega})$ satisfy $\rho(x), \mu(x) \geq \alpha_0 > 0$. Then the forward problem for the single component measured displacement is assumed to be modeled by the following wave equation based on the reasons given in [22]:

$$\nabla \cdot (\mu(\vec{x}) \nabla u(\vec{x}, t)) = \rho(\vec{x}) u_{tt}(\vec{x}, t) \quad \text{in } \Omega \times (0, T), \quad (1)$$

where in general in this paper $\Omega \subset \mathbb{R}^n (n = 2, 3)$ is the half space $\Omega = \{\vec{x} = (x, \hat{x}); \hat{x} \in \mathbb{R}^{n-1}, n = 2, 3, x > 0\}$.

To be consistent with the experiments, we assume that either a single frequency continuous excitation is on the boundary or the broadband pulse has a central frequency:

$$u(\vec{x}, 0) = u_t(\vec{x}, 0) = 0 \quad \text{on } \Omega, \quad (2)$$

$$u(\vec{x}, t) = f(\vec{x}, t) \quad \text{on } \partial\Omega \times (0, T) \quad (3)$$

or

$$\mu(\vec{x}) \nabla u(\vec{x}, t) \cdot \nu(\vec{x}) = g(\vec{x}, t) \quad \text{on } \partial\Omega \times (0, T), \quad (4)$$

where $g(\vec{x}, t)$ is the boundary excitation we will use later for the forward simulation. To be consistent with the experimental setup introduced in section 1, $f(\vec{x}, t)$ or $g(\vec{x}, t)$ will have a central frequency 50–200 Hz and will be a smooth function compactly supported in $\vec{x} \in \partial\Omega$ and $t \in (0, T)$.

2.2. Inverse problem model

Here, we make the commonly accepted assumption that $\rho(x)$ is a constant. Then our target in the inverse problem is to identify the ratio of the shear modulus $\mu(x)$ to ρ , $\mu/\rho = \tilde{\mu}$.

$$\begin{aligned} \nabla \cdot (\mu(\vec{x}) \nabla u(\vec{x}, t)) &= \rho(\vec{x}) u_{tt}(\vec{x}, t), \quad \tilde{\mu} = \frac{\mu}{\rho} \Rightarrow \\ \nabla \cdot (\tilde{\mu}(\vec{x}) \nabla u(\vec{x}, t)) &= u_{tt}(\vec{x}, t). \end{aligned} \quad (5)$$

In the inverse problem models we consider here, we use frequency content in the measured data. Starting from equation (5), we take the Fourier transform on both sides of the equation and select the central frequency frame as we expect the displacement there to have maximum information content. Denoting ω_c as the central frequency, we get

$$\left. \begin{aligned} \nabla \cdot (\tilde{\mu}(\vec{x}) \nabla u(\vec{x}, t)) &= u_{tt}(\vec{x}, t) \\ \hat{u}(\vec{x}, \omega) &= \frac{1}{\sqrt{2\pi}} \int_{-\infty}^{+\infty} e^{-i\omega t} u(\vec{x}, t) dt \end{aligned} \right\} \Rightarrow$$

$$\begin{aligned} \nabla \cdot (\tilde{\mu}(\vec{x}) \nabla \hat{u}(\vec{x}, \omega_c)) &= -\omega_c^2 \hat{u}(\vec{x}, \omega_c) \Rightarrow \\ \nabla \tilde{\mu}(\vec{x}) \cdot \nabla \hat{u}(\vec{x}, \omega_c) + \tilde{\mu}(\vec{x}) \Delta \hat{u}(\vec{x}, \omega_c) + \omega_c^2 \hat{u}(\vec{x}, \omega_c) &= 0. \end{aligned} \quad (6)$$

For the inverse problem model, (6) is the correct equation to use and we call it the full inversion model. However, a widely accepted concept is to assume homogeneity in a local

volume for shear modulus μ and remove the terms containing $\nabla \tilde{\mu}$ from (6), then we will arrive at

$$\hat{\mu}(\vec{x})\Delta\hat{u}(\vec{x}, \omega_c) + \omega_c^2\hat{u}(\vec{x}, \omega_c) = 0. \quad (7)$$

In this case the approximated $\tilde{\mu}$, which we denote by $\hat{\mu}$, can be recovered at each spatial point by simple algebra, we call this method the direct inversion model.

As our measured data is two dimensional, we use a 2D formulation for gradient and Laplacian. This is only valid if our solution is nearly constant in the out of the image plane direction, z , in which case if we let $\vec{x} = (x, \hat{x}) = (x, y, z)$

$$\left| \frac{\partial^2 \hat{u}}{\partial z^2} \right| \ll \left| \frac{\partial^2 \hat{u}}{\partial x^2} + \frac{\partial^2 \hat{u}}{\partial y^2} \right|, \quad \left| \frac{\partial \hat{u}}{\partial z} \right| \ll \left| \frac{\partial \hat{u}}{\partial x} \right| + \left| \frac{\partial \hat{u}}{\partial y} \right|.$$

If this assumption is not valid, our experience is that we obtain overshoot in our reconstruction. However, the experiments are designed to achieve this approximation.

The direct inversion model is valid in areas where $\tilde{\mu}$ is constant. For variable $\tilde{\mu}$, this leaves open the possibility of producing inaccurate results. However, our analysis and simulation results in the next two sections show that the relative difference between the recovery, $\hat{\mu}$, from the direct inversion model and exact ratio, $\tilde{\mu}$, is quantifiably small in most cases. We do, however, exhibit examples to show when the locally constant assumption results in invalid reconstructions.

3. Error estimate for direct inversion approximation in 2D

3.1. Mathematical model for relative error

Equation (6), which is a first-order partial differential equation, is the correct model to apply in the inverse problem as it is consistent with the forward problem model (1). However, for first-order partial differential equations, information flow is along characteristic directions and here the directions are determined by $\nabla \hat{u}$. This can be problematic in parts of the domain Ω where the direction of characteristic curves changes dramatically. In addition, for equation (6) an assumption about $\tilde{\mu}$ must be made on part of the boundary of the domain. Equation (7) is local and straightforward, but neglecting the first derivative term necessarily implies inaccurate results where $\tilde{\mu}$ changes. In order to choose a good approximation model with fast and easy implementation, we need to compare the recoveries from (6) and (7). The relative difference between those two reconstructions is derived as follows:

$$\left. \begin{aligned} \hat{\mu}\Delta\hat{u} + \omega^2\hat{u} = 0 \\ \nabla\tilde{\mu} \cdot \nabla\hat{u} + \tilde{\mu}\Delta\hat{u} + \omega^2\hat{u} = 0 \\ \hat{\mu}\Delta\hat{u} + \omega^2\hat{u} = 0 \end{aligned} \right\} \implies \left. \begin{aligned} \Delta\hat{u} = -\frac{\omega^2\hat{u}}{\hat{\mu}} \\ (\tilde{\mu} - \hat{\mu})\Delta\hat{u} + \nabla\tilde{\mu} \cdot \nabla\hat{u} = 0 \end{aligned} \right\} \implies$$

$$-\omega^2\hat{u}(\tilde{\mu} - \hat{\mu})\frac{1}{\hat{\mu}} + \nabla\tilde{\mu} \cdot \nabla\hat{u} = 0 \implies$$

$$\frac{\tilde{\mu} - \hat{\mu}}{\hat{\mu}} = \frac{\nabla\tilde{\mu} \cdot \nabla\hat{u}}{\omega^2\hat{u}} \implies$$

$$\left| \frac{\tilde{\mu}(x_0) - \hat{\mu}(x_0)}{\hat{\mu}(x_0)} \right| \leq |\nabla\tilde{\mu}(x_0)| \frac{1}{\omega^2} \left| \frac{\nabla\hat{u}(x_0)}{\hat{u}(x_0)} \right|. \quad (8)$$

To quantify the relative difference, our target is to replace the expression

$$\frac{1}{\omega^2} \left| \frac{\nabla\hat{u}(x)}{\hat{u}(x)} \right|$$

in (8) by a function of ω only. In order to accomplish this goal, we use both the complex \hat{u} and separate its real and imaginary parts. Separating the complex Fourier transformed data as $\hat{u} = M \exp(i\phi) = u_r + iu_i$, we shall have from (6) that

$$\tilde{\mu} \Delta u_r + \nabla \tilde{\mu} \cdot \nabla u_r + \omega^2 u_r = 0, \quad (9)$$

$$\tilde{\mu} \Delta u_i + \nabla \tilde{\mu} \cdot \nabla u_i + \omega^2 u_i = 0. \quad (10)$$

In the following section we will establish that, $\exists C(\omega, D) > 0, \forall x_0 \in \Omega$ and $\Omega' = B_D(x_0) \in \Omega, D > 0$, such that

$$\begin{aligned} |\nabla u_r(x_0)| &\leq C(\omega, D) \max_{\Omega'} |u_r(x_0)| \leq C(\omega, D) \max_{\Omega'} M \\ |\nabla u_i(x_0)| &\leq C(\omega, D) \max_{\Omega'} |u_i(x_0)| \leq C(\omega, D) \max_{\Omega'} M, \end{aligned} \quad (11)$$

where C is a constant independent of x_0 . Then by using

$$|\nabla \hat{u}(x_0)| = \sqrt{|\nabla u_r(x_0)|^2 + |\nabla u_i(x_0)|^2} \leq \sqrt{2} C(\omega, D) \max_{\Omega'} M$$

we can show that the relative difference (8) can be quantitatively measured as

$$\begin{aligned} \left| \frac{\tilde{\mu}(x_0) - \hat{\mu}(x_0)}{\hat{\mu}(x_0)} \right| &\leq |\nabla \tilde{\mu}(x_0)| \frac{1}{\omega^2} \left| \frac{\nabla \hat{u}(x_0)}{\hat{u}(x_0)} \right| \\ &\leq |\nabla \tilde{\mu}(x_0)| \frac{1}{\omega^2} \frac{\sqrt{2} C(\omega, D) \max_{\Omega'} M}{|\hat{u}(x_0)|} \\ &\leq \frac{\sqrt{2} C(\omega, D) \max_{\Omega'} M}{\omega^2 M(x_0)} |\nabla \tilde{\mu}(x_0)|. \end{aligned} \quad (12)$$

3.2. Bound for relative error

The fundamental lemma in this section establishes (11) in 2D. The proof of this lemma is given in the appendix.

Lemma 1. Suppose $u(x)$ is $u_i(x)$ or $u_r(x)$ and is a \mathbb{C}^2 solution of the elliptic equation (9) or (10) in $\Omega \subset \mathbb{R}^2$. If we assume

$$\min_{\Omega'} \tilde{\mu} \geq 1, \quad \max_{\Omega'} |\nabla \tilde{\mu}| \leq 20, \quad \omega \geq \omega_0 = 200\pi, \quad (13)$$

then

$$|\nabla u(x_0)| \leq C(\omega, D) \max_{\Omega'} M, \quad (14)$$

where

$$C(\omega, D) = \frac{10}{D} \left[3 + 2 \left(|\log 2D| + \frac{1}{\pi} \right) (20D + 1) D^2 \omega^2 \right]$$

for $\forall x_0 \in \Omega$ and $\Omega' = B_D(x_0) \subset \Omega, D = \frac{1}{\omega} > 0$.

Remark 1.

- The assumption $D = \frac{1}{\omega}$ is purely a number operation while other choices could be made. Here we chose D to be the spatial wavelength when the wave speed is 1 m s^{-1} .
- In our applications the frequency content is in the range of 50–300 Hz (i.e. cycles per second). Our results apply when the cycles per second are greater than or equal to 100 Hz.

As the constant C in (11) has been established by (14), a further quantification on the relative difference (12) can be made.

Theorem 1. *If all assumptions in lemma 1 are satisfied and $\max_{\Omega'} M/M(x_0) \leq 2$, then*

$$\left| \frac{\tilde{\mu}(x_0) - \hat{\mu}(x_0)}{\hat{\mu}(x_0)} \right| \leq 70 \frac{|\log \omega|}{\omega} |\nabla \tilde{\mu}(x_0)|. \quad (15)$$

Proof. Let us denote

$$\bar{C} = \frac{\sqrt{2}C}{\omega^2} = \frac{10\sqrt{2}}{D\omega^2} \left[3 + 2 \left(|\log 2D| + \frac{1}{\pi} \right) (20D + 1) D^2 \omega^2 \right].$$

Again, assuming that $D = 1/\omega$, the constant \bar{C} can be bounded as

$$\begin{aligned} \bar{C} &\leq 10\sqrt{2} \left[\frac{3}{\omega} + 2 \left(\frac{1}{\omega} \left| \log \frac{2}{\omega} \right| + \frac{1}{\pi\omega} \right) \left(\frac{20}{\omega} + 1 \right) \right] \\ &= \frac{10\sqrt{2}}{\omega} \left[3 + 2 \left(\left| \log \frac{2}{\omega} \right| + \frac{1}{\pi} \right) \left(\frac{20}{\omega} + 1 \right) \right] \\ &= \frac{10\sqrt{2} |\log \omega|}{\omega} \left[\frac{3}{|\log \omega|} + 2 \left(\left| \frac{\log 2}{\log \omega} - 1 \right| + \frac{1}{\pi |\log \omega|} \right) \left(\frac{20}{\omega} + 1 \right) \right]. \end{aligned}$$

Set

$$h_1(\omega) = \frac{|\log \omega|}{\omega}, \quad h_2(\omega) = \frac{3}{|\log \omega|} + 2 \left(\left| \frac{\log 2}{\log \omega} - 1 \right| + \frac{1}{\pi |\log \omega|} \right) \left(\frac{20}{\omega} + 1 \right).$$

Recall the assumption $\omega \geq \omega_0 = 200\pi$ from (13) and take the derivative of $h_i(\omega)$, $i = 1, 2$, with respect to ω , we get

$$h_1'(\omega) < 0, \quad h_2'(\omega) < 0.$$

Then $h_i(\omega)$, $i = 1, 2$, are decreasing functions of ω and we get

$$10\sqrt{2}h_2(\omega) = 10\sqrt{2} \left[\frac{3}{|\log \omega|} + 2 \left(\left| \frac{\log 2}{\log \omega} - 1 \right| + \frac{1}{\pi |\log \omega|} \right) \left(\frac{20}{\omega} + 1 \right) \right] \leq 35 \implies$$

$$\bar{C} < 35 \frac{|\log \omega|}{\omega} \implies$$

$$\left| \frac{\tilde{\mu}(x_0) - \hat{\mu}(x_0)}{\hat{\mu}(x_0)} \right| \leq 35 \frac{\max_{\Omega'} M}{M(x_0)} \frac{|\log \omega|}{\omega} |\nabla \tilde{\mu}(x_0)|.$$

The ratio between $\max_{\Omega'} M$ and $M(x_0)$ can be computed for each point, \vec{x} , over the whole domain from data once D is determined, which is the case here. Specifically, our results apply to the situation where $M(x_0) > 0$. If we restrict to subdomains where

$$\frac{\max_{\Omega'} M}{M(x_0)} \leq 2$$

then the final estimate of the relative difference is

$$\left| \frac{\tilde{\mu}(x_0) - \hat{\mu}(x_0)}{\hat{\mu}(x_0)} \right| \leq 70 \frac{|\log \omega|}{\omega} |\nabla \tilde{\mu}(x_0)|.$$

This completes the proof. \square

A number of observations can be deduced from (15):

- the bound on the relative difference has a frequency dependence, the relative error will decrease as ω increases;

- we could calculate a bound for $\max_{\Omega} M/M(x_0)$ for all $x_0 \in \Omega$ and all possible solutions of (6) by using the Moser iteration combined with the John–Nirenberg result (see [15]). However, this would be a very large bound since we would be including nonphysical solutions. Instead we can calculate the bound based on data. In our experience this value satisfies our assumption;
- the bound on the relative difference between $\hat{\mu}$ and $\tilde{\mu}$ is a unitless measure. This can be proven by showing that the fundamental solution, or Green’s function, for the Laplace operator is unitless in \mathbb{R}^2 .

Now we have established and quantified a bound on the relative error between the recovery $\hat{\mu}$ and exact ratio $\tilde{\mu}$. We will test our theoretical results on the relative difference in the next two sections by reconstructing $\tilde{\mu}$ from synthetic data using the direct inversion (7).

4. Forward simulation, implementation of the direct inversion method and numerical error control

4.1. Simulation setup and absorbing boundary condition implementation

For the numerical simulation of our forward problem in space/time, we generate data by solving (1), (2) and (4) for $u(\vec{x}, t)$, using a fourth-order finite difference scheme in the interior of the 2D domain: $\Omega = \{\vec{x} = (x, y) \in \mathbb{R}^2 : 0 \leq x \leq 0.05, -0.025 \leq y \leq 0.025\}$. The units we use are seconds for time, meters for length, m s^{-1} for speed and the constant density is picked as $\rho = 1000 \text{ kg/m}^3$. The Neumann boundary condition on top of the domain, $x = 0$, is given by

$$\frac{\partial u}{\partial x}(y, 0, t) = \frac{1}{2\sqrt{\pi}c_t} \cos(\omega(t - t_0)) \exp\left[-\frac{(t - t_0)^2}{2c_t^2}\right],$$

where we choose $t_0 = 0.05$, $c_t = 0.01$ and $\omega = 200\pi$. The rapid decay of the temporal Gaussian above makes the amplitude of the source function drop below machine precision after a short time. This enables us to simulate a short duration wave pulse.

For all the numerical examples presented in this paper, the simulation is stopped at $t_{\max} = 0.1125 \text{ s}$ and the interior of the 2D domain is discretized into a 101×101 spatial grid. We do this to simulate the discretization in the experiments.

The forward problem model (1) is established in a half space while the simulation for it can only be performed in the truncated domain Ω . In order to prevent the numerical reflections of outgoing waves from the boundaries of the finite computational domain, we need to use appropriate boundary conditions. In [11], Collino and Tsogka introduced the perfectly matched absorbing layer model (PML) by the split-field approach for a general hyperbolic system. The idea is to surround the domain of interest by some artificial absorbing layers in which waves are trapped and attenuated. In our case, layers are added on the left side, right side and bottom of Ω (see figure 1). The setup of the first-order system that is solved in the layer follows the derivation in [11].

The numerical simulation presented in this paper makes use of fourth-order operators in the interior region and second-order operators in the PML region. In the region near the PML interface, the operators are allowed to overlap. From the fourth-order interior region, our numerical scheme samples two nodes in the PML region. Similarly, the second-order PML scheme samples one node into the interior domain. Due to this mixing of operators, fourth-order accuracy cannot be achieved as the second-order numerical error propagates from the absorbing layer back to the interior domain. In addition, Collino and Tsogka have shown in [11] that artificial reflections from the PML regions are generated by the dispersion of the

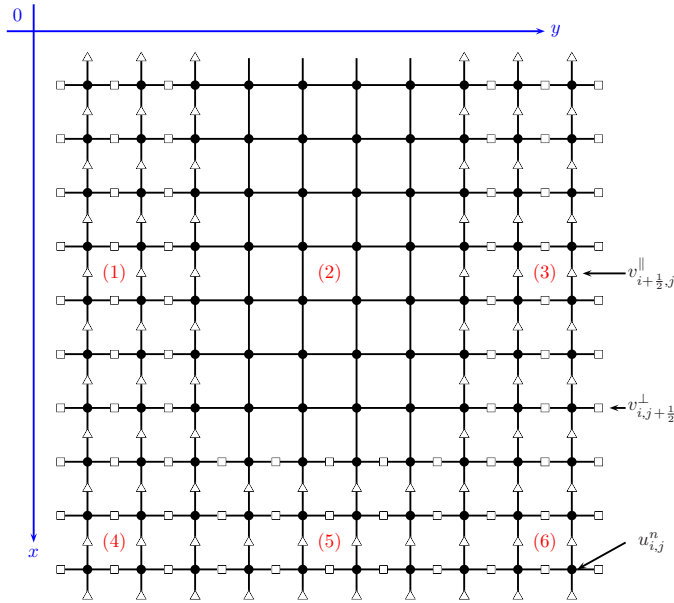


Figure 1. Spatial discretization in the computational domain: areas (1), (3)–(6) represent the absorbing layers while area (2) is the interior domain; $v_{i+\frac{1}{2},j}^{\parallel}$ and $v_{i,j+\frac{1}{2}}^{\perp}$ represent the split field solutions in the layer.

finite difference scheme. As high-order operators have the effect of mitigating numerical dispersions, the application of a fourth-order scheme in the PML could be expected to have increased absorptions. Thus the development and implementation of a fourth-order numerical scheme in the PML regions remains as an important part of future work. Nevertheless, we still get good reconstruction results from our simulation data.

4.2. Numerical implementation of the direct inversion scheme and numerical error control for this scheme

An inverse crime occurs in the inverse problem when the same theoretical ingredients are used to simulate and subsequently invert data to reconstruct the target parameters. To avoid an inverse crime, we then use a different mesh for the inverse problem than that used to simulate the data. The displacement data on the new mesh is generated by a two-dimensional cubic spline interpolation from the simulated data on the old mesh and the new grid size is two-thirds of the grid size used in the forward simulation. To reconstruct $\tilde{\mu}$, we first Fourier transform the two-dimensional interpolated data and pick out the central frequency frame. We then need to apply appropriate numerical operators in the direct inversion model. Recall equation (6):

$$\nabla \tilde{\mu}(x) \cdot \nabla \hat{u}(x, \omega_c) + \tilde{\mu}(x) \Delta \hat{u}(x, \omega_c) + \omega_c^2 \hat{u}(x, \omega_c) = 0.$$

As the targeted quantity $\tilde{\mu}$ is real, we need to extract a real equation from the complex model first. We separate phase and amplitude of the complex data as $\hat{u} = M e^{i\phi}$, rewrite the derivatives of \hat{u} in terms of derivatives of M and ϕ , then factor out $e^{i\phi}$ and pick out the real part of the resulting equation:

$$\nabla \tilde{\mu} \cdot \nabla \hat{u} + \tilde{\mu} \Delta \hat{u} + \omega_c^2 \hat{u} = 0, \quad \hat{u} = M e^{i\phi} \Rightarrow \{ (M_x + iM\phi_x) \tilde{\mu}_x + (M_y + iM\phi_y) \tilde{\mu}_y$$

$$\begin{aligned}
& + [\Delta M - |\nabla\phi|^2 M + i(2\nabla M \nabla\phi + M \Delta\phi)]\tilde{\mu} + \omega_c^2 M \} e^{i\phi} = 0 \Rightarrow \\
& M_x \tilde{\mu}_x + M_y \tilde{\mu}_y + \tilde{\mu}(\Delta M - |\nabla\phi|^2 M) + \omega_c^2 M = 0.
\end{aligned} \tag{16}$$

Under the locally constant assumption for $\tilde{\mu}$, (16) can be reduced to the direct inversion model by eliminating the derivative terms of $\tilde{\mu}$ and we get the equation to solve for the direct inversion solution $\hat{\mu}$:

$$\hat{\mu}[\Delta M - |\nabla\phi|^2 M] + \omega^2 M = 0. \tag{17}$$

For (17), we separate the amplitude and phase of the Fourier transformed data on the new mesh and apply eighth-order finite difference numerical schemes to compute spatial derivatives of M and ϕ . Now $\hat{\mu}$ can be recovered at each spatial point \vec{x} by simple algebra from (17).

Before presenting the reconstructed images from synthetic data, we address the issue of numerical error in the inverse problem recovery. The error comes from the combination of truncation error, machine roundoff error and the numerical routine of the fast Fourier transform. The total error can be minimized by choosing optimal spatial and temporal step sizes in the forward simulation. The main analytical results for using second-order central difference discretization in the inverse problems are given below.

Recall the forward model equation (1):

$$\nabla \cdot (\mu(\vec{x}) \nabla u(\vec{x}, t)) = \rho(\vec{x}) u_{tt}(\vec{x}, t).$$

In areas where the shear modulus and the density are constant, the forward model effectively reduces to the 2D wave equation

$$\rho u_{tt} = \mu \Delta u. \tag{18}$$

Recall the direct inversion scheme (7),

$$\hat{\mu} \Delta \hat{u} + \omega^2 \hat{u} = 0,$$

which is the Fourier transform of (18). If we denote the finite difference approximation for $\Delta \hat{u}$ as $\Delta \hat{u}_d$ and the numerical reconstruction for $\hat{\mu}$ as $\hat{\mu}_d$, then we calculate the error, $\hat{\mu} - \hat{\mu}_d$, as

$$\begin{aligned}
& \left. \begin{aligned} \hat{\mu} \Delta \hat{u} + \omega^2 \hat{u} &= \hat{\mu} \Delta \hat{u}_d - \hat{\mu} Err_{\text{inverse}} + \omega^2 \hat{u} = 0 \\ \hat{\mu}_d \Delta \hat{u}_d + \omega^2 \hat{u} &= 0 \end{aligned} \right\} \Rightarrow \\
& \hat{\mu} \Delta \hat{u}_d - \hat{\mu} Err_{\text{inverse}} - \hat{\mu}_d \Delta \hat{u}_d = 0 \Rightarrow \\
& \hat{\mu} - \hat{\mu}_d = \frac{\hat{\mu} Err_{\text{inverse}}}{\Delta \hat{u}_d},
\end{aligned}$$

where $Err_{\text{inverse}} = \Delta \hat{u}_d - \Delta \hat{u}$ denotes the truncation error introduced by the application of the finite difference operators. In order to minimize the effect of numerical error so that we can get the best reconstructions for $\hat{\mu}$, optimal step sizes need to be chosen correspondingly in the forward simulation. The statements of the main results are given in the following proposition:

Proposition 1. Suppose the solution for (18) is in the form of

$$u = \exp(-i\omega x/\sqrt{2\mu}) \exp(-i\omega y/\sqrt{2\mu}) \exp(i\omega t). \tag{19}$$

Consider the Courant–Friedrichs–Lewy condition $dx = dy = m\sqrt{\mu} dt$, $m \in \mathbb{N}$ and denote machine roundoff error as ϵ , the error introduced by using a second-order finite difference scheme to approximate spatial derivatives in the direct inversion scheme is

$$Err_{\text{inverse},2\text{nd}} = Tm\sqrt{\mu} \left(\frac{\omega^4 \Delta x}{24\mu} + \mu \frac{8\epsilon}{\Delta x^3} \right). \tag{20}$$

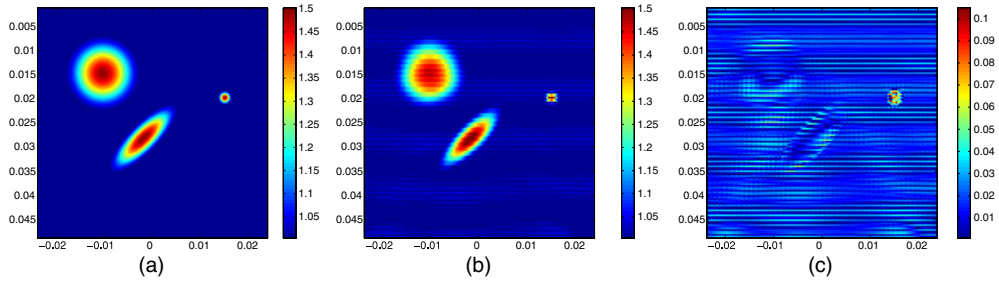


Figure 2. (a) Exact shear modulus: a circular inclusion of radius 8 mm, a circular inclusion of radius 1.5 mm and a tilted ellipse inclusion in constant background, (b) direct inversion recovery and (c) the relative difference between the exact value and the reconstruction.

The optimal error and step sizes can then be calculated and given by

$$dx_{\text{optimal, inverse, 2nd}} = \frac{2\sqrt{\mu}}{\omega} \sqrt{36\epsilon}.$$

The proof of this proposition can be carried out by using typical machine error analysis in finite difference formulae with simple extreme point finding in calculus. Based on this analytical result on numerical error control, we can pick appropriate step sizes in the forward simulation with specific parameter settings for μ and ω to minimize the effect of numerical error. At the same time, we also have to take into consideration the practical experimental settings for spatial step sizes. An accurate simulation and the best feasible reconstruction can then be achieved in the forward and the inverse problem. The numerical results are presented next.

5. Exact and approximate inversion results

Now we test the performance of the direct inversion method by utilizing equation (17) on simulated data in two numerical examples and show the consistency of our reconstructions with the bound established in theorem 1. We will show that if $|\nabla\tilde{\mu}|$ is not too large, then the direct inversion performs well. If not, the direct inversion result can be very inaccurate.

For the first example, we have constant shear modulus $\mu = 1$ KPa in most parts of the interior domain while there are inclusions defined by polynomial functions: one circular inclusion of radius 8 mm, another circular inclusion of radius 1.5 mm and one tilted ellipse inclusion. The highest point of the inclusions is 1.5 times higher than the constant background. The exact modulus, the direct inversion recovery and the relative difference of the reconstruction are shown in figure 2. Both the support and the value of three inclusions are very well reconstructed. The biggest relative difference is about 10%, which is well below the theoretical bound of the relative error. This example clearly shows that the direct inversion scheme can create excellent reconstructions for $\tilde{\mu}$. Since we interpolated the synthetic data to a new mesh with comparable step sizes of the practical experimental settings, which are not the optimal step sizes (see proposition 1 in the last section), the numerical error resulting from the interpolation and the inverse scheme is not negligible in parts of the domain where the exact shear modulus is constant and the direct inversion recoveries have 1% error in those areas.

In our second simulation example, we have one circular inclusion defined by polynomial functions of radius 5 mm located in the right side of the domain. The highest point of the inclusion is now 12 times higher than the constant background, which makes the gradient

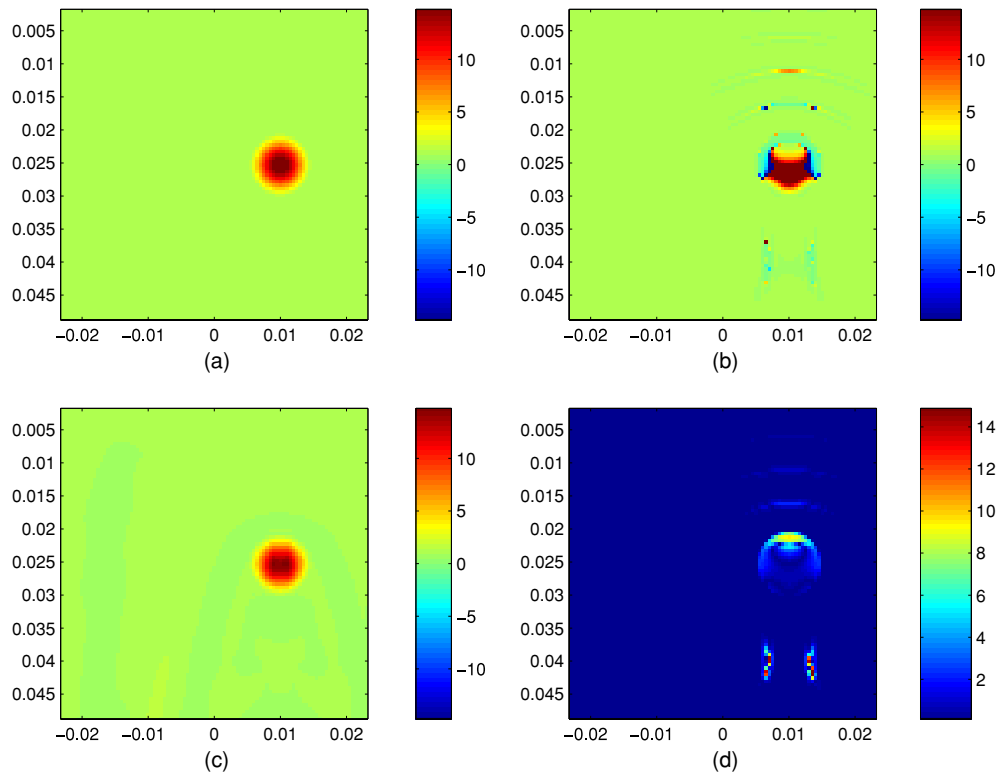


Figure 3. (a) Exact shear modulus: a circular polynomial inclusion of radius 5 mm in the right side of the constant background, (b) direct inversion recovery, (c) reconstruction by a nonlinear numerical scheme for solving the PDE (6) and (d) the relative difference between the exact value and the direct inversion reconstruction.

of the exact modulus much higher than the assumption of the theoretical bound. The exact modulus, the direct inversion recovery, a reconstruction by a nonlinear partial differential equation solver, which is presented in [20], and the relative error of the direct inversion are given in figure 3. The recovery by the direct inversion captures the location of the inclusion but contains quite a few artifacts inside the inclusion and in the background, which produces huge relative error. On the other hand, the recovery by the differential equation solver captures the support and the value of the high inclusion perfectly. This means that once the shear modulus changes rapidly, the direct inversion method is no longer a perfectly reliable solver to reconstruct the target parameter and more attention should be paid to the numerical solver of the correct model (6) in the inverse problem.

6. Conclusion and future work

In this paper, we investigate the locally constant assumption for the shear modulus in the inverse problem model. We derive the formula for the relative difference between the solution from the simplified inverse problem model, direct inversion, and the exact value of shear modulus. A theoretical bound on the relative error is established and confirmed by numerical reconstructions from simulated data. We conclude that it is appropriate to apply the direct inversion model in the inverse problem under the condition that the exact shear modulus is not

changing too rapidly and the frequency of the signal used in the experiments is above a certain level.

There are several issues to address in future work:

- the relative error estimate needs to be extended to the case for the full elastic system;
- robust numerical schemes to recover $\tilde{\mu}$ from the first order p.d.e. model (6) are presented in [20].

Acknowledgments

We have benefited from discussions with D Schwendeman, A Maniatty, A Oberai, P Zheglova. KL and JM were partially supported by ONR Grant Nos. N000 14-05-1-0600 and N000 14-08-1-0432, and NIBIB Grant No. 1R21EB003000-01 and NIBIB Grant No. R01AG029804.

Appendix. Proof for the fundamental lemma

For all $x \in \tilde{\Omega}$, which may be any proper open subset of \mathbb{R}^2 , let us write $d_x = \text{dist}(x, \partial\tilde{\Omega})$. We define for $u \in \mathbb{C}^k(\tilde{\Omega})$ the following norms and seminorms:

$$|u|_{0;\tilde{\Omega}} = \max_{x \in \tilde{\Omega}} |u(x)| \quad (\text{A.1})$$

$$[u]_{k;\tilde{\Omega}}^* = \max_{x \in \tilde{\Omega}, |\beta|=k} d_x^k |D^\beta u(x)|, \quad k = 0, 1, 2, \dots \quad (\text{A.2})$$

We then recall equation (9) with u_r replaced by u :

$$\tilde{\mu}\Delta u + \nabla\tilde{\mu} \cdot \nabla u + \omega^2 u = 0.$$

For all $x_0 \in \Omega$, the equation above can be regarded as a local perturbation of the following constant coefficient equation:

$$\begin{aligned} \tilde{\mu}(x_0)\Delta u &= [\tilde{\mu}(x_0) - \tilde{\mu}(x)]\Delta u - \nabla\tilde{\mu} \cdot \nabla u - \omega^2 u := F(x) \implies \\ \Delta u &= \frac{1}{\tilde{\mu}(x_0)} F(x) = \tilde{F}(x), \quad \text{in } B_D(x_0) = \Omega' \subset \Omega, \end{aligned} \quad (\text{A.3})$$

which means u is also a solution for the Poisson equation (A.3). Our approach in this proof is to: first establish a bound on $d_x |\nabla u(x)|$, $\forall x \in \Omega'$ in terms of $|u|_{0;\Omega'}$ and $[u]_{1;\Omega'}^*$; then take the maximum of $d_x |\nabla u(x)|$ and choose appropriate D to set up the bound on $[u]_{1;\Omega'}^*$ in terms of $|u|_{0;\Omega'}$; the final estimate follows naturally as $D|\nabla u(x_0)|$ is bounded by $[u]_{1;\Omega'}^*$.

At $\forall \hat{x} \in \Omega'$, we decompose $u(x) = v(x) + w(x)$ in $B_{2R}(\hat{x})$, $R = \theta d_{\hat{x}}$, $4R < 1$, $\theta \leq \frac{1}{3}$, $d_{\hat{x}} = \text{dist}(\hat{x}, \partial\Omega')$ (see figure A1), where $v(x)$ is harmonic in $B_{2R}(\hat{x})$ and $w(x)$ is the Newtonian potential of $\tilde{F}(x)$ in the same small region, this decomposition comes from the Green's formula:

$$u(y) = \int_{\partial B_{2R}(\hat{x})} \left[u \frac{\partial \Gamma}{\partial n}(x-y) - \Gamma(x-y) \frac{\partial u}{\partial n} \right] ds + \int_{B_{2R}(\hat{x})} \Gamma(x-y) \Delta u \, dx, \quad y \in B_{2R}(x_0)$$

where

$$\Gamma(x-y) = \Gamma(|x-y|) = \begin{cases} \frac{1}{n(2-n)\omega_n} |x-y|^{2-n}, & n > 2 \\ \frac{1}{2\pi} \log|x-y|, & n = 2. \end{cases}$$

$\omega_n = \frac{2\pi^{n/2}}{n\Gamma(n/2)}$: volume of unit ball in \mathbb{R} . In our case we consider $n = 2$. The bound on $d_{\hat{x}} |\nabla u|$ will be achieved by bounding ∇v and ∇w .

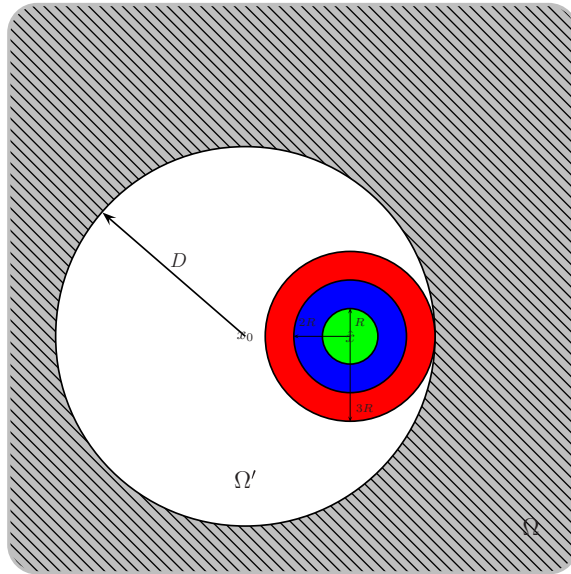


Figure A1. Graphical illustration of sub domain set up, $\forall x_0 \in \Omega$.

Following a similar approach as in [15], we can carry on the estimate as

$$\begin{aligned}
 d_{\hat{x}} |\nabla u(\hat{x})| &\leq \frac{1}{\theta} R |\nabla u|_{0; B_R(\hat{x})} \\
 &\leq \frac{1}{\theta} R |\nabla v|_{0; B_R(\hat{x})} + \frac{1}{\theta} R |\nabla w|_{0; B_R(\hat{x})}.
 \end{aligned}
 \tag{A.4}$$

To bound $|D_i w|_{0; B_R(\hat{x})}$, we start from its own definition:

$$\begin{aligned}
 |D_i w|_{0; B_R(\hat{x})} &= \max_{y \in B_R(\hat{x})} \left| \int_{B_{2R}(\hat{x})} D_i \Gamma(x - y) \tilde{F}(x) \, dx \right| \\
 &\leq |\tilde{F}|_{0; B_{2R}(\hat{x})} \frac{1}{2\pi} \max_{y \in B_R(\hat{x})} \int_{B_{2R}(\hat{x})} \frac{|x_i - y_i|}{(x_1 - y_1)^2 + (x_2 - y_2)^2} \, dx.
 \end{aligned}$$

Then we evaluate the integral

$$\int_{B_{2R}(\hat{x})} \frac{|x_i - y_i|}{(x_1 - y_1)^2 + (x_2 - y_2)^2} \, dx.$$

Changing from Cartesian coordinates to polar coordinates where the origin is set to be the point y , the transformation is defined as follows:

$$\begin{aligned}
 x_1 - y_1 &= r \cos \theta, & x_2 - y_2 &= r \sin \theta, \\
 (x_1 - y_1)^2 + (x_2 - y_2)^2 &= r^2.
 \end{aligned}$$

Then if we denote

$$r_s = \text{dist}(y, \partial B_{2R}(\hat{x})), \quad r_l = 2R - \text{dist}(y, \partial B_{2R}(\hat{x}))$$

we can get an estimate on the integral as

$$\begin{aligned} & \int_{B_{2R}(\hat{x})} \frac{|x_1 - y_1|}{(x_1 - y_1)^2 + (x_2 - y_2)^2} dx \\ &= \int_{B_{r_s}(y)} \frac{|x_1 - y_1|}{(x_1 - y_1)^2 + (x_2 - y_2)^2} dx \\ &+ \int_{B_{2R}(\hat{x}) - B_{r_s}(y)} \frac{|x_1 - y_1|}{(x_1 - y_1)^2 + (x_2 - y_2)^2} dx \\ &= \int_0^{2\pi} \int_0^{r_s} \frac{r |\cos \theta|}{r^2} r dr d\theta + \int_{B_{2R}(\hat{x}) - B_{r_s}(y)} \frac{r |\cos \theta|}{r^2} r dr d\theta \\ &\leq r_s \int_0^{2\pi} |\cos \theta| d\theta + \int_{B_{2R}(\hat{x}) - B_{r_s}(y)} |\cos \theta| dr d\theta \\ &\leq (r_s + 2R - r_s) \int_0^{2\pi} |\cos \theta| d\theta = 8R, \end{aligned}$$

which gives the estimate on ∇w as

$$|D_i w|_{0; B_R(\hat{x})} \leq \frac{4R}{\pi} |\tilde{F}|_{0; B_{2R}(\hat{x})}.$$

To set up an estimate on ∇v , we note that $v(x)$ is harmonic. By theorem 2.10 (see [15]), \forall domains $\Omega_1 \subset \Omega_2 \subseteq B_{2R}(\hat{x})$,

$$\begin{aligned} \max_{\Omega_1} |D^\alpha v| &\leq \left(\frac{n|\alpha|}{d}\right)^{|\alpha|} \max_{\Omega_2} |v|, \quad d = \text{dist}(\Omega_1, \partial\Omega_2) \implies \\ |\nabla v|_{0; B_R(\hat{x})} &\leq \frac{2}{R} |v|_{0; B_{2R}(\hat{x})}. \end{aligned} \tag{A.5}$$

By the maximum principle of harmonic functions, we get

$$\begin{aligned} |v|_{0; B_{2R}(\hat{x})} &\leq |v|_{0; \partial B_{2R}(\hat{x})} \\ &\leq |u|_{0; \partial B_{2R}(\hat{x})} + |w|_{0; \partial B_{2R}(\hat{x})} \\ &\leq |u|_{0; B_{2R}(\hat{x})} + |w|_{0; \partial B_{2R}(\hat{x})}. \end{aligned} \tag{A.6}$$

We now need to estimate $|w|_{0; \partial B_{2R}(\hat{x})}$. Recall the definition of w :

$$\begin{aligned} |w| &= \left| \int_{B_{2R}(\hat{x})} \Gamma(x - y) \Delta u dx \right| = \left| \int_{B_{2R}(\hat{x})} \Gamma(x - y) \tilde{F} dx \right| \\ &\leq |\tilde{F}|_{B_{2R}(\hat{x})} \left| \int_{B_{2R}(\hat{x})} \Gamma(x - y) dx \right|. \end{aligned} \tag{A.7}$$

In 2D, let $2R - \epsilon > 0$

$$\begin{aligned} \left| \int_{B_{2R}(\hat{x})} \Gamma(x - y) dx \right| &= \frac{1}{2\pi} \left| \int_{B_{2R}(\hat{x})} \log |x - y| dx \right| \\ &\leq \frac{1}{2\pi} \left| \int_{B_{2R-\epsilon}(\hat{x})} \log |x - y| dx \right| \\ &+ \frac{1}{2\pi} \left| \int_{B_{2R}(\hat{x}) - B_{2R-\epsilon}(\hat{x})} \log |x - y| dx \right| \end{aligned} \tag{A.8}$$

$$= I_1 + I_2. \tag{A.9}$$

The decomposition of this integration can be graphically illustrated by figure A2, the basic idea is to isolate the singular part of the integral and treat it separately.

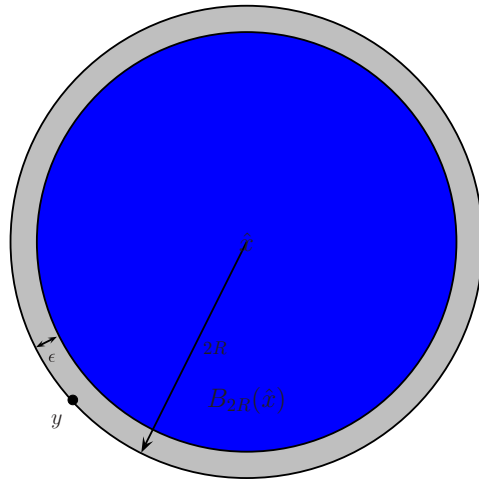


Figure A2. Graphical illustration for the integral domain setup of $I_1 + I_2$.

The integral (A.9) is calculated as follows: first, by the mean value theorem of harmonic functions,

$$\begin{aligned}
 I_1 &= \pi(2R - \epsilon)^2 \frac{1}{2\pi} |\log 2R| \\
 &= \frac{(2R - \epsilon)^2}{2} |\log 2R| \Rightarrow \frac{(2R)^2}{2} |\log 2R|, \quad \text{as } \epsilon \rightarrow 0. \quad (\text{A.10})
 \end{aligned}$$

Transforming to polar coordinates, i.e. $x - \hat{x} = (r \cos \theta, r \sin \theta)$ and noticing that in the shell $B_{2R}(\hat{x}) - B_{2R-\epsilon}(\hat{x})$, we have

$$1 > |x - y| \geq 2R - r \implies |\log |x - y|| \leq |\log(2R - r)|,$$

then

$$\begin{aligned}
 I_2 &\leq \frac{1}{2\pi} \left| \int_{B_{2R}(\hat{x}) - B_{2R-\epsilon}(\hat{x})} \log(2R - r) \, dx \right| \\
 &= \frac{1}{2\pi} \left| \int_0^{2\pi} \int_{2R-\epsilon}^{2R} r \log(2R - r) \, dr \, d\theta \right| \\
 &= \left| \left[\frac{(2R - r)^2}{2} \log(2R - r) - \frac{(2R - r)^2}{4} \right. \right. \\
 &\quad \left. \left. - 2R(2R - r) \log(2R - r) - 2Rr \right] \right|_{2R-\epsilon}^{2R} \\
 &= \left| -(2R)^2 - \frac{\epsilon^2}{2} \log \epsilon + \frac{\epsilon^2}{4} + 2R\epsilon \log \epsilon + (2R)^2 - 2R\epsilon \right| \\
 &\rightarrow 0, \quad \text{as } \epsilon \rightarrow 0. \quad (\text{A.11})
 \end{aligned}$$

Using (A.7)–(A.11), we get

$$|w|_{0; \partial B_{2R}(\hat{x})} \leq \frac{(2R)^2}{2} |\log 2R| |\tilde{F}|_{0; B_{2R}(\hat{x})}. \quad (\text{A.12})$$

Combining (A.4)–(A.7), (A.12) and also changing $\tilde{F} = F/\tilde{\mu}(x_0)$, we accomplish a bound as

$$\begin{aligned} d_{\hat{x}}|Du(\hat{x})| &\leq \frac{1}{\theta}R\frac{2}{R}|v|_{0;B_{2R}(\hat{x})} + \frac{4R^2}{\theta\pi}|\tilde{F}|_{0;B_{2R}(\hat{x})} \\ &\leq \frac{2}{\theta}|v|_{0;B_{2R}(\hat{x})} + \frac{4R^2}{\theta\pi}|\tilde{F}|_{0;B_{2R}(\hat{x})} \\ &\leq \frac{2}{\theta}|u|_{0;B_{2R}(\hat{x})} + \frac{(2R)^2|\log 2R|}{\theta\tilde{\mu}(x_0)}|F|_{0;B_{2R}(\hat{x})} + \frac{4R^2}{\theta\tilde{\mu}(x_0)\pi}|F|_{0;B_{2R}(\hat{x})}. \end{aligned}$$

We proceed to estimate $|F|_{0;B_{2R}(\hat{x})}$ in terms of $|u|_{0;\Omega'}$ and $[u]_{1;\Omega'}^*$. Recall the definition of F : $F(x) = [\tilde{\mu}(x_0) - \tilde{\mu}(x)]\Delta u - \nabla\tilde{\mu} \cdot \nabla u - \omega^2 u$, and a simple algebra relation: $\Delta u = \frac{1}{\tilde{\mu}(x)}(-\nabla\tilde{\mu} \cdot \nabla u - \omega^2 u)$, then the following inequality is derived:

$$\begin{aligned} R|F|_{0;B_{2R}(\hat{x})} &\leq R|[\tilde{\mu}(x_0) - \tilde{\mu}(x)]\Delta u|_{0;B_{2R}(\hat{x})} + R|\nabla\tilde{\mu} \cdot \nabla u|_{0;B_{2R}(\hat{x})} + \omega^2 R|u|_{0;B_{2R}(\hat{x})} \\ &\leq R\left|\frac{\tilde{\mu}(x_0) - \tilde{\mu}(x)}{\tilde{\mu}(x)}\right|_{0;B_{2R}(\hat{x})} (|\nabla\tilde{\mu}|_{0;B_{2R}(\hat{x})}|\nabla u|_{0;B_{2R}(\hat{x})} + \omega^2|u|_{0;B_{2R}(\hat{x})}) \\ &\quad + R|\nabla\tilde{\mu}|_{0;B_{2R}(\hat{x})}|\nabla u|_{0;B_{2R}(\hat{x})} + R\omega^2|u|_{0;B_{2R}(\hat{x})} \\ &\leq \left(\left|\frac{\tilde{\mu}(x_0) - \tilde{\mu}(x)}{\tilde{\mu}(x)}\right|_{0;B_{2R}(\hat{x})} + 1\right) R|\nabla\tilde{\mu}|_{0;B_{2R}(\hat{x})}|\nabla u|_{0;B_{2R}(\hat{x})} \\ &\quad + R\omega^2\left(\left|\frac{\tilde{\mu}(x_0) - \tilde{\mu}(x)}{\tilde{\mu}(x)}\right|_{0;B_{2R}(\hat{x})} + 1\right)|u|_{0;B_{2R}(\hat{x})}. \end{aligned}$$

Since $R|\nabla u|_{0;B_{2R}(\hat{x})} \leq [u]_{1;B_{3R}(\hat{x})}^* \leq [u]_{1;\Omega'}^*$, we can expand the norm from the small neighborhood of \hat{x} to the whole domain Ω' in the formula above,

$$\begin{aligned} R|F|_{0;B_{2R}(\hat{x})} &\leq \left(\left|\frac{\tilde{\mu}(x_0) - \tilde{\mu}(x)}{\tilde{\mu}(x)}\right|_{0;\Omega'} + 1\right) |\nabla\tilde{\mu}|_{0;\Omega'} [u]_{1;\Omega'}^* \\ &\quad + \frac{D\omega^2}{3} \left(\left|\frac{\tilde{\mu}(x_0) - \tilde{\mu}(x)}{\tilde{\mu}(x)}\right|_{0;\Omega'} + 1\right) |u|_{0;\Omega'}. \end{aligned}$$

Now let $\lambda = \min_{\Omega} \tilde{\mu}(x)$ and recall $3R \leq D \Rightarrow R \leq D/3$, we obtain

$$\begin{aligned} d_{\hat{x}}|\nabla u(\hat{x})| &\leq \frac{2}{\theta}|u|_{0;\Omega'} + \left(\frac{4D|\log 2D|}{3\theta\lambda} + \frac{4D}{3\pi\theta\lambda}\right) \left(\left|\frac{\tilde{\mu}(x_0) - \tilde{\mu}(x)}{\tilde{\mu}(x)}\right|_{0;\Omega'} + 1\right) \\ &\quad \times |\nabla\tilde{\mu}|_{0;\Omega'} [u]_{1;\Omega'}^* + \frac{D^2\omega^2}{\theta\lambda} \left(\frac{4}{9}|\log 2D| + \frac{4}{9\pi}\right) \left(\left|\frac{\tilde{\mu}(x_0) - \tilde{\mu}(x)}{\tilde{\mu}(x)}\right|_{0;\Omega'} + 1\right) |u|_{0;\Omega'}. \end{aligned}$$

As \hat{x} is chosen arbitrarily in Ω' , it follows by taking the maximum over all points in Ω' that

$$\begin{aligned} [u]_{1;\Omega'}^* &\leq \frac{2}{\theta}|u|_{0;\Omega'} + \left(\frac{4D|\log 2D|}{3\theta\lambda} + \frac{4D}{3\pi\theta\lambda}\right) \left(\left|\frac{\tilde{\mu}(x_0) - \tilde{\mu}(x)}{\tilde{\mu}(x)}\right|_{0;\Omega'} + 1\right) |\nabla\tilde{\mu}|_{0;\Omega'} [u]_{1;\Omega'}^* \\ &\quad + \frac{D^2\omega^2}{\theta\lambda} \left(\frac{4}{9}|\log 2D| + \frac{4}{9\pi}\right) \left(\left|\frac{\tilde{\mu}(x_0) - \tilde{\mu}(x)}{\tilde{\mu}(x)}\right|_{0;\Omega'} + 1\right) |u|_{0;\Omega'}. \quad (\text{A.13}) \end{aligned}$$

The next step is to determine the sizes of D , λ and $|\nabla\tilde{\mu}|_{0;\Omega'}$ such that the upper bound on $[u]_{1;\Omega'}^*$ can be established. We now denote

$$g(D) = \left(\frac{4D|\log 2D|}{3\theta\lambda} + \frac{4D}{3\pi\theta\lambda} \right) \left(\left| \frac{\tilde{\mu}(x_0) - \tilde{\mu}(x)}{\tilde{\mu}(x)} \right|_{0;\Omega'} + 1 \right) |\nabla\tilde{\mu}|_{0;\Omega'}$$

and (A.13) is changed to

$$(1 - g(D))[u]_{1;\Omega'}^* \leq \frac{2}{\theta}|u|_{0;\Omega'} + \frac{D^2\omega^2}{\theta\lambda} \left(\frac{4}{9}|\log 2D| + \frac{4}{9\pi} \right) \left(\left| \frac{\tilde{\mu}(x_0) - \tilde{\mu}(x)}{\tilde{\mu}(x)} \right|_{0;\Omega'} + 1 \right) |u|_{0;\Omega'}.$$

A necessary condition to estimate $[u]_{1;\Omega'}^*$ is that $g(D) < 1$. Let us assume

$$\lambda = \min_{\Omega'} \tilde{\mu} \geq 1, \quad |\nabla\tilde{\mu}|_{0;\Omega'} \leq 20, \quad \theta = \frac{1}{3}, \quad (\text{A.14})$$

which gives us

$$\begin{aligned} \left| \frac{\tilde{\mu}(x_0) - \tilde{\mu}(x)}{\tilde{\mu}(x)} \right|_{0;\Omega'} &= \max_{\Omega'} \left| \frac{\tilde{\mu}(x_0) - \tilde{\mu}(x)}{\tilde{\mu}(x)} \right| \leq \frac{D}{\lambda} |\nabla\tilde{\mu}|_{0;\Omega'} \leq 20D \Rightarrow \\ g(D) &\leq 80D \left(|\log 2D| + \frac{1}{\pi} \right) (20D + 1). \end{aligned} \quad (\text{A.15})$$

We further set

$$f(D) = 80D \left(|\log 2D| + \frac{1}{\pi} \right) (20D + 1).$$

Take the first derivative of $f(D)$ for $0 \leq 2D \leq e^{-1}$, we get

$$f'(D) = \left(|\log 2D| + \frac{1}{\pi} \right) (3200D + 80) - 80(20D + 1),$$

then $f'(D) \geq 0$. If we assume $\omega \geq \omega_0 = 200\pi$, which corresponds to frequency 100 Hz, then $\forall x_0 \in \Omega$ with a subdomain $B_D(x_0) = \Omega' \subset \Omega$ such that $D = \frac{1}{2}\text{diam}\Omega' = \frac{1}{\omega} \leq \frac{1}{\omega_0} = D_0 < 1/(2e)$, we establish

$$\begin{aligned} g(D) &\leq f(D) = f\left(\frac{1}{\omega}\right) \leq f\left(\frac{1}{\omega_0}\right) = f(D_0) = 0.8 \Rightarrow \\ 1 - g(D) &\geq \frac{1}{5} \Rightarrow \frac{1}{1 - g(D)} \leq 5. \end{aligned}$$

With the bound on $\frac{1}{1-g(D)}$ and all the parameter settings (A.14) and (A.15), we obtain

$$\begin{aligned} D|\nabla u(x_0)| &\leq \max_{\Omega'} d_x |\nabla u(x)| \\ &= [u]_{1;\Omega'}^* \\ &\leq \frac{2}{(1 - g(D))\theta} |u|_{0;\Omega'} + \frac{(\frac{4}{3}|\log 2D| + \frac{4}{3\pi})}{(1 - g(D))\theta\lambda} \left(\left| \frac{\tilde{\mu}(x_0) - \tilde{\mu}(x)}{\tilde{\mu}(x)} \right|_{0;\Omega'} + 1 \right) |u|_{0;\Omega'} D^2\omega^2 \\ &\leq 30|u|_{0;\Omega'} + 20 \left(|\log 2D| + \frac{1}{\pi} \right) (20D + 1) |u|_{0;\Omega'} D^2\omega^2 \Rightarrow \\ |\nabla u(x_0)| &\leq \frac{10}{D} \left[3 + 2 \left(|\log 2D| + \frac{1}{\pi} \right) (20D + 1) D^2\omega^2 \right] |u|_{0;\Omega'}. \end{aligned} \quad (\text{A.16})$$

The proof for the fundamental lemma is now complete.

References

- [1] Bercoff J, Chaffai S, Tanter M, Sandrin L, Fink M, Gennisson J L and Meunier M 2003 In vivo breast tumor detection using transient elastography *Ultrasound Med. Biol.* **29** 1387–96
- [2] Bercoff J, Tanter M and Fink M 2004 Supersonic shear imaging: a new technique for soft tissue elasticity mapping *IEEE Trans. Ultrason. Ferroelectr. Freq. Control* **19** 396–409
- [3] Bercoff J, Muller M, Tanter M and Fink M 2001 Studying viscoelasticity in soft tissues with supersonic shear imaging *J. Acoust. Soc. Am.* **115** 2411–2
- [4] Bercoff J, Pernot M, Tanter M and Fink M 2004 Monitoring thermally-induced lesions with supersonic shear imaging *Ultrason. Imaging* **26** 71–84
- [5] Bercoff J, Tanter M, Chaffai S, Sandrin L and Fink M 2002 Ultrafast imaging of beamformed shear waves induced by acoustic radiation force: application to transient elastography *IEEE Ultrason. Symp. Proc.* vol 2, pp 1899–902
- [6] Bercoff J, Tanter M, Catheline S and Fink M 2001 Ultrafast compound imaging of 2D displacement vector measurements: application to transient elastography and color flow mapping *IEEE Ultrason. Symp. Proc.* vol 2, pp 1619–22
- [7] Catheline S, Bercoff J, Gennisson J L, Barriere C and Fink M 2004 Nonlinearity studies in soft tissues with the supersonic shear imaging system *IEEE Ultrason. Symp.* **2** 1510–2
- [8] Catheline S, Gennisson J L, Delon G, Fink M, Sinkus R, Abouelkaram S and Culioli J 2004 Measurement of viscoelastic properties of homogeneous soft solid using transient elastography: an inverse problem approach *J. Acoust. Soc. Am.* **116** 3734–41
- [9] Catheline S, Thomas J-L, Wu F and Fink M 1999 Diffraction field of a low frequency vibrator in soft tissues using transient elastography *IEEE Trans. Ultrason. Ferroelectr. Freq. Control* **46** 1013–9
- [10] Ehman R L, Manduca A, McLaughlin J R, Renzi D and Yoon J-R 2006 Variance controlled shear stiffness images for MRE data *IEEE Int. Symp. Biomed. Imaging: Macro to Nano* 960–3
- [11] Francis C and Chryssoula T 2001 Application of the perfectly matched layer model to the linear elastodynamic problem in anisotropic heterogeneous media *Geophysics* **66** 294–307
- [12] Fink M, Sandrin L, Tanter M, Catheline S, Chaffai S, Bercoff J and Gennisson J L 2002 Ultra high speed imaging of elasticity *IEEE Ultrason. Symp.* **2** 1811–20
- [13] Greenleaf J F, Muthupillai R, Rossman P J, Smith J, Manduca A and Ehman R L 1996 Direct visualization of strain waves by magnetic resonance elastography (MRE) 1996 *IEEE Ultrason. Symp. Proc.* vol 1, pp 467–72
- [14] Gao L, Parker K J and Alam S K 1995 Sonoelasticity imaging: theory and experimental verification *J. Acoust. Soc. Am.* **97** 3875–80
- [15] Gilbarg D and Trudinger N S 1997 *Elliptic Partial Differential Equations of Second Order* 3rd edn (Berlin: Springer)
- [16] Konafagou E E, Harrigan T and Ophir J 2000 Shear strain estimation and lesion mobility assessment in elastography *Ultrasonics* **38** 400–04
- [17] Konafagou E E 2000 Precision estimation and imaging of shear and normal components of 3D strain tensor in elastography *Phys. Med. Biol.* **45** 1553–63
- [18] Konafagou E E and Ophir J 1998 A new elastographic method for estimation and imaging of lateral displacements, lateral strains, corrected axial strains and Poisson's ratios in tissues *Ultrasound Med. Biol.* **24** 1183–99
- [19] Konafagou E E, Varghesse T and Ophir J 2000 Theoretical bounds on the estimation of transverse displacement, transverse strain and Poisson's ratios in elastography *Ultrason. Imaging* **22** 153–77
- [20] Lin K, McLaughlin J and Zhang N Log-elastographic and non-marching full inversion schemes for shear modulus recovery from single frequency elastographic data *Inverse Problems* **25** 075004
- [21] Manduca A, Oliphant T E, Mahowald J L, Kruse S A, Amromin E, Felmlee J P, Greenleaf J F and Ehman R L 2001 Magnetic resonance elastography: non-invasive mapping of tissue elasticity *Med. Image Anal.* **5** 237–54
- [22] McLaughlin J R and Renzi D 2006 Shear wave speed recovery in transient elastography and supersonic imaging using propagating fronts *Inverse Problems* **22** 681–706
- [23] Oliphant T E, Kinnick R R, Manduca A, Ehman R L and Greenleaf J F 2000 An error analysis of Helmholtz inversion for incompressible shear, vibration elastography with application to filter-design for tissue characterization *IEEE Ultrason. Symp.* **2** 1795–8
- [24] Oliphant T E, Manduca A, Ehman R L and Greenleaf J F 2001 Complex-valued stiffness reconstruction for magnetic resonance elastography by algebraic inversion of the differential equation *Magn. Reson. Med.* **45** 299–310
- [25] Sinkus R, Siegmann K, Xydeas T, Tanter M, Claussen C and Fink M 2007 MR elastography of breast lesions: understanding the solid/liquid duality can improve the specificity of contrast-enhanced MR mammography *Magn. Reson. Med.* **58** 1135–44

- [26] Sandrin L, Tanter M, Catheline S and Fink M 2002 Shear modulus imaging with 2-D transient elastography *IEEE Trans. Ultrason. Ferroelectr. Freq. Control* **49** 426–35
- [27] Sandrin L, Tanter M, Gennisson J L, Catheline S and Fink M 2001 Shear elasticity probe in soft tissue with 1-D transient elastography *IEEE Trans. Ultrason. Ferroelectr. Freq. Control* **49** 436–46
- [28] Sinkus R, Tanter M, Xydeas T, Catheline S, Bercoff J and Fink M 2005 Viscoelastic shear properties of in vivo breast lesions measured by MR Elastography *Magn. Reson. Imaging* **23** 159–65
- [29] Tanter M, Bercoff J, Sandrin L and Fink M 2002 Ultrafast compound umaging for 2D motion vector estimation: application to transient elastography *IEEE Trans. Ultrason. Ferroelectr. Freq. Control* **49** 1363–74
- [30] Tayler L S, Porter B C, Rubens D J and Parker K J 2000 Three-dimensional sonoelasticity: principles and practices *Phys. Med. Biol.* **45** 1477–94
- [31] Van Houten E, Doyley M, Kennedy F, Weaver J and Paulsen K 2003 Initial *in vivo* experience with steady-state subzone-based MR elastography of the human breast *J. Magn. Reson. Imaging* **17** 72–85
- [32] Van Houten E, Miga M, Weaver J, Kennedy F and Paulsen K 2001 Three-dimensional subzone-based reconstruction algorithm for MR elastography *Magn. Reson. Med* **45** 827–37
- [33] Van Houten E, Paulsen K, Miga M, Kennedy F and Weaver J 1999 An overlapping sub-zone technique for MR-based elastic property reconstruction *Magn. Reson. Med* **42** 779–86
- [34] Van Houten E, Weaver J, Miga M, Kennedy F and Paulsen K 2000 Elasticity reconstruction from experimental MR displacement data: initial experience with an overlapping subzone finite element inversion process *Med. Phys.* **27** 101–7
- [35] Wu Z, Rubens D J and Parker K J 2006 Sonoelastographic imaging of interference patterns for estimation of shear velocity distribution in biomaterial *J. Acoust. Soc. Am.* **120** 535–45
- [36] Wu Z, Taylor L S, Rubens D J and Parker K J 2002 Shear wave focusing for three-dimensional sonoelastography *J. Acoust. Soc. Am.* **111** 439–46
- [37] Wu Z, Taylor L S, Rubens D J and Parker K J 2004 Sonoelastographic imaging of interference patterns for estimation of shear velocity of homogeneous biomaterials *Phys. Med. Biol.* **49** 911–22